Monthly Notices
of the
ROYAL ASTRONOMICAL SOCIETY

Mon. Not. R. Astron. Soc. **411,** 1409–1417 (2011) doi:10.1111/j.1365-2966.2010.17746.x

Refined molecular gas mass and star-formation efficiency in NGC 3627

Y. Watanabe,[1,2⋆] K. Sorai,[1] N. Kuno[3,4] and A. Habe[1]

[1]*Department of Physics, Graduate School of Science, Hokkaido University, Kita 10 Nishi 8, Sapporo 060-0810, Japan*
[2]*Department of Physics, Graduate School of Science, The University of Tokyo, 7-3-1 Hongo, Bunkyo-ku, Tokyo 113-0033, Japan*
[3]*Nobeyama Radio Observatory, National Astronomical Observatory of Japan, Minamimaki-mura, Minamimaki-gun, Nagano 384-1305, Japan*
[4]*The Graduate University for Advanced Studies (SOKENDAI), 2-21-1 Osawa, Mitaka, Tokyo 181-0015, Japan*

Accepted 2010 September 17. Received 2010 August 19; in original form 2009 December 14

ABSTRACT

We present a ^{13}CO ($J = 1$–0) mapping observation of the nearby barred spiral galaxy NGC 3627, covering almost all the stellar disc, with the Nobeyama 45-m telescope. We found that the ^{13}CO ($J = 1$–0) morphology of NGC 3627 is similar to the ^{12}CO ($J = 1$–0) map and the ^{12}CO ($J = 1$–0)/^{13}CO ($J = 1$–0) intensity ratio is 10.7 ± 0.4 on average. We also found that the ratio varies position-to-position in the galaxy and decreases with the galactocentric distance. The ratio is especially high, $\sim$20, in the bar and this result suggests that the molecular gas mass calculated from the ^{12}CO ($J = 1$–0) intensity with constant conversion factor is overestimated in the bar. As a result, the star-formation efficiency (SFE) in the bar, which is derived from ^{13}CO ($J = 1$–0) intensity, is similar to that in the other regions except for the two bar ends and the centre. We found that the SFE is higher in the bar ends than in the other regions. We discuss plausible reasons for the enhanced SFE in the bar: the kinetic temperature of the molecular gas, the spatial gap between the molecular gas peak and star formation and gravitational instability.

Key words: galaxies: individual: NGC 3627 – galaxies: ISM – galaxies: spiral – radio lines: galaxies.

1 INTRODUCTION

Barred spiral galaxies are ideal sources for studying the relation between star formation on small scales (i.e. 10–100 pc molecular clouds and complexes) and kpc-scale galactic dynamics and gas kinematics. The non-axisymmetric bar potential induces non-circular motions of stars and gas in the bar. Many theoretical studies and numerical simulations have shown that these motions pile up the gas along the leading side of the bar and induce shock waves and/or shear motion (e.g. Roberts, Huntley & van Albada 1979; Athanassoula 1992). Such an environment associated with the gas motion under the bar potential is expected to change the physical properties of gas in the bar. The shock wave and the shear motion make molecular clouds break down, which eventually suppresses the star-formation activities in the bar. Observational studies have shown that the star-formation rate (SFR) in the bar is lower than in the spiral arms, despite there being much molecular gas in the bar (e.g. Reynaud & Downes 1998; Sheth et al. 2000). In other words, star-formation efficiency (SFE), which is derived by dividing SFR by the gas mass and represents the inverse of gas depletion time by star formation, is lower in the bar.

To better understand star formation under kpc-scale motion in a galaxy, it is important to investigate the physical properties of the molecular gas that is the raw material of stars. In addition to ^{12}CO ($J = 1$–0) observations, observations of other transition lines and other molecular species are necessary to achieve this, since ^{12}CO ($J = 1$–0) is too optically thick to estimate the physical states inside the molecular cloud. Some studies based on other molecular lines than ^{12}CO ($J = 1$–0) have revealed that the molecular gas properties in the bar are different from those in the remaining disc region. Hüttemeister et al. (2000) observed the barred galaxy NGC 7479 in ^{12}CO ($J = 1$–0) and ^{13}CO ($J = 1$–0) lines with the Owens Valley Radio Observatory millimetre-wavelength array and found that the ^{12}CO ($J = 1$–0)/^{13}CO ($J = 1$–0) ratio ($R_{12/13}$) varies from a typical value for the galactic disc (about 5) to larger than 30. They interpreted this variation in terms of the relative importance of the contribution of diffuse molecular gas, characterized by gravitationally unbound gas with a moderate optical depth in ^{12}CO ($J = 1$–0).

In this paper, we present mapping observations of the ^{13}CO ($J = 1$–0) transition line in barred spiral galaxy NGC 3627. The galaxy is classified as SABb in the Third Reference Catalog of Bright Galaxies (RC3; de Vaucouleurs et al. 1991) and the nuclear activity is LINER/type 2 Seyfert (Ho, Filippenko & Sargent 1997). An optical image of NGC 3627 shows a slight asymmetric structure in the spiral arms. Haynes, Giovanelli & Roberts (1979) suggested that NGC 3627 experienced an interaction with NGC 3628, from the distorted structure observed in the H I gas. Several CO mapping observations had been performed (Reuter et al. 1996; Helfer et al.

⋆E-mail: nabe@taurus.phys.s.u-tokyo.ac.jp

Table 1. Parameters of the observations.

Object name	NGC 3627
α_{J2000}	$11^h20^m15\overset{s}{.}027$
δ_{J2000}	$+12^\circ59'29\overset{''}{.}58$
V_{LSR}	715 km s^{-1}
Map grid spacing	$10\overset{''}{.}3$
Map PA	176°
X-grid range	($92\overset{''}{.}7$, $-103\overset{''}{.}0$)
Y-grid range	($-103\overset{''}{.}0$, $92\overset{''}{.}7$)

2003; Kuno et al. 2007) and revealed that much of the molecular gas is associated with the central region, the bar and the spiral arms. Its inclination angle of ∼60° allows us to resolve the position-to-position molecular gas properties and star-formation activity in the galaxy.

This paper is structured as follows: in Section 2 we present the observations and data reduction; our results are given in Section 3. We compare ^{12}CO ($J = 1$–0) and ^{13}CO ($J = 1$–0) data in Section 4, and we discuss molecular gas and star formation in Section 5. Finally, we give our conclusions in Section 6.

2 OBSERVATION

We conducted a ^{13}CO ($J = 1$–0) transition line (rest frequency of 110.201353 GHz) observation of NGC 3627 in 2007 May and 2008 April with the 45-m telescope of Nobeyama Radio Observatory (NRO). A half-power beam width (HPBW) is ∼16 arcsec, which corresponds to ∼800 pc if a distance of NGC 3627 of 11.1 Mpc (Saha et al. 1999) is assumed. All 400 positions were observed with the same observation grid as the Nobeyama CO Atlas (Kuno et al. 2007). We used 25 (5×5) SIS receivers BEARS (the 25-BEam Array Receiver System). As a backend we used 25 digital spectrometers (Sorai et al. 2000) with total bandwidth of 512 MHz and frequency resolution of 605 kHz centred on the frequency corresponding to the local standard of rest (LSR) receding velocity. The observed intensity was corrected for atmospheric and antenna ohmic losses through the position-switching method and converted into antenna temperature T_A^* through the chopper-wheel method. To calibrate variations between the 25 receivers and to correct the double-side-band (DSB) intensity into the single-side-band (SSB) intensity, we applied scaling factors to the observed T_A^*; these factors were obtained by NRO by observing a standard source with each beam and with a single beam receiver S100 equipped with a SSB filter. The system noise temperatures were 600–1000 K on the SSB T_A^* scale during the observation. The telescope pointing was checked every hour by observing nearby SiO maser source R Leo, which ensured pointing errors lower than 5 arcsec. The integration time of a scan was 20 s and the total integration time was typically 50 min at each position. The observation parameters are summarized in Table 1.

We reduced the data obtained with NEWSTAR, a software package based on AIPS, which was developed by NRO. Base lines of spectra were subtracted by fitting linear or second-order polynomial curves. Distorted spectra, due to bad conditions of the atmosphere or devices and which cannot be extracted by fitting linear or second-order polynomial curves, were removed before integration. The integrated spectra obtained were smoothed to a velocity resolution of 20 km s^{-1}. The antenna temperature scale was converted to a main beam temperature T_{mb} via T_A^*/η_{mb}, where η_{mb} was the main beam efficiency of the 45-m telescope and here we used $\eta_{mb} = 0.31$. The final r.m.s. noise resolution was typically 6–16 mK on a T_{mb}^* scale at 20 km s^{-1} resolution.

3 RESULTS

Fig. 1 shows zeroth-moment (integrated intensity), first-moment (intensity-weighted mean velocity) and second-moment (intensity-weighted velocity dispersion) maps. Fig. 1(d) shows the observed positions and a definition of the galactic structures, called the central region, bar, bar ends, offset stream where the emission runs off toward the leading side of the stellar bar, and the spiral arms, since we discuss the properties of molecular gas with respect to specific structures.

Fig. 1(a) shows that ^{13}CO ($J = 1$–0) emission is distributed along the position where ^{12}CO ($J = 1$–0) has been detected. At the two bar ends the characteristic intensity peaks that appeared in ^{12}CO ($J = 1$–0) also appear in ^{13}CO ($J = 1$–0).

As Regan, Sheth & Vogel (1999) have mentioned, the large velocity dispersion is recognizable at the bar and tends to be especially large at the southern bar (Fig. 1c). Fig. 1(c) also shows that the eastern spiral arm shows larger velocity dispersion than the western one, as Reuter et al. (1996) have suggested.

4 COMPARISONS OF ^{13}CO($J = 1$–0) AND ^{12}CO($J = 1$–0)

Optically thin ^{13}CO ($J = 1$–0) emission can trace molecular gas mass more precisely than optically thick ^{12}CO ($J = 1$–0) emission, since most ^{12}CO ($J = 1$–0) emission emerges from the surface of a molecular cloud. We compare our ^{13}CO ($J = 1$–0) data with the previous ^{12}CO ($J = 1$–0) data taken by Kuno et al. (2007).

4.1 Positional variation of ^{12}CO($J = 1$–0) to ^{13}CO($J = 1$–0) ratio

We compare the ^{13}CO ($J = 1$–0) integrated intensity, $I_{13} \equiv \int T_{mb}(^{13}\mathrm{CO})\,\mathrm{d}v$, with the ^{12}CO ($J = 1$–0) integrated intensity I_{12}. The errors in I_{12} and I_{13}, ΔI_{12} and ΔI_{13}, caused by rms noise are estimated as $\Delta I = \sqrt{(\Delta T_{mb})^2 \Delta v\,\mathrm{d}v}$, where ΔT_{mb} is the r.m.s noise temperature on a T_{mb} scale, Δv is the velocity interval for the integration and dv is the velocity resolution.

In this analysis, no correction derived from the different beam sizes of ^{12}CO ($J = 1$–0) and ^{13}CO ($J = 1$–0), ∼16 arcsec and ∼17 arcsec respectively, was applied to I_{12} and I_{13}. Although ∼10 per cent of correction to $R_{12/13}(\equiv I_{12}/I_{13})$ is necessary for a point source emission, this is comparable to the uncertainty due to ΔI_{12} and ΔI_{13}. As the source extends within the observation beam, the necessary correction would be smaller. Hence, the beam-filling factors are necessary for accurate correction.

In Fig. 2, which shows the relationships between I_{13} and I_{12}, a weak correlation is found with a coefficient of 0.65. A mean value of $R_{12/13}$ is 10.7 ± 0.4, which was given by the least-squares-fitting straight line. Plots of the central region and the bar are distributed in the upper left area of Fig. 2 and $R_{12/13}$ is expected to be large in these regions.

The average $R_{12/13}$ of 10.7 ± 0.4 is similar to the values measured in the previous observations of nearby spiral galaxies (e.g. Sage & Isbell 1991; Paglione et al. 2001), but larger than the Galactic values of ∼2–5. The discrepancy of $R_{12/13}$ in nearby galaxies and the Milky Way is possibly caused by the spatial resolution of observations. In the case of CO observations of external galaxies, the observation beams subtend a larger area than the size of molecular clouds and the diffuse envelope, which emits ^{12}CO but is very weak ^{13}CO, would be contained within the beams. On the other hand, in the case of CO observations of the Milky Way, observation beams usually resolve

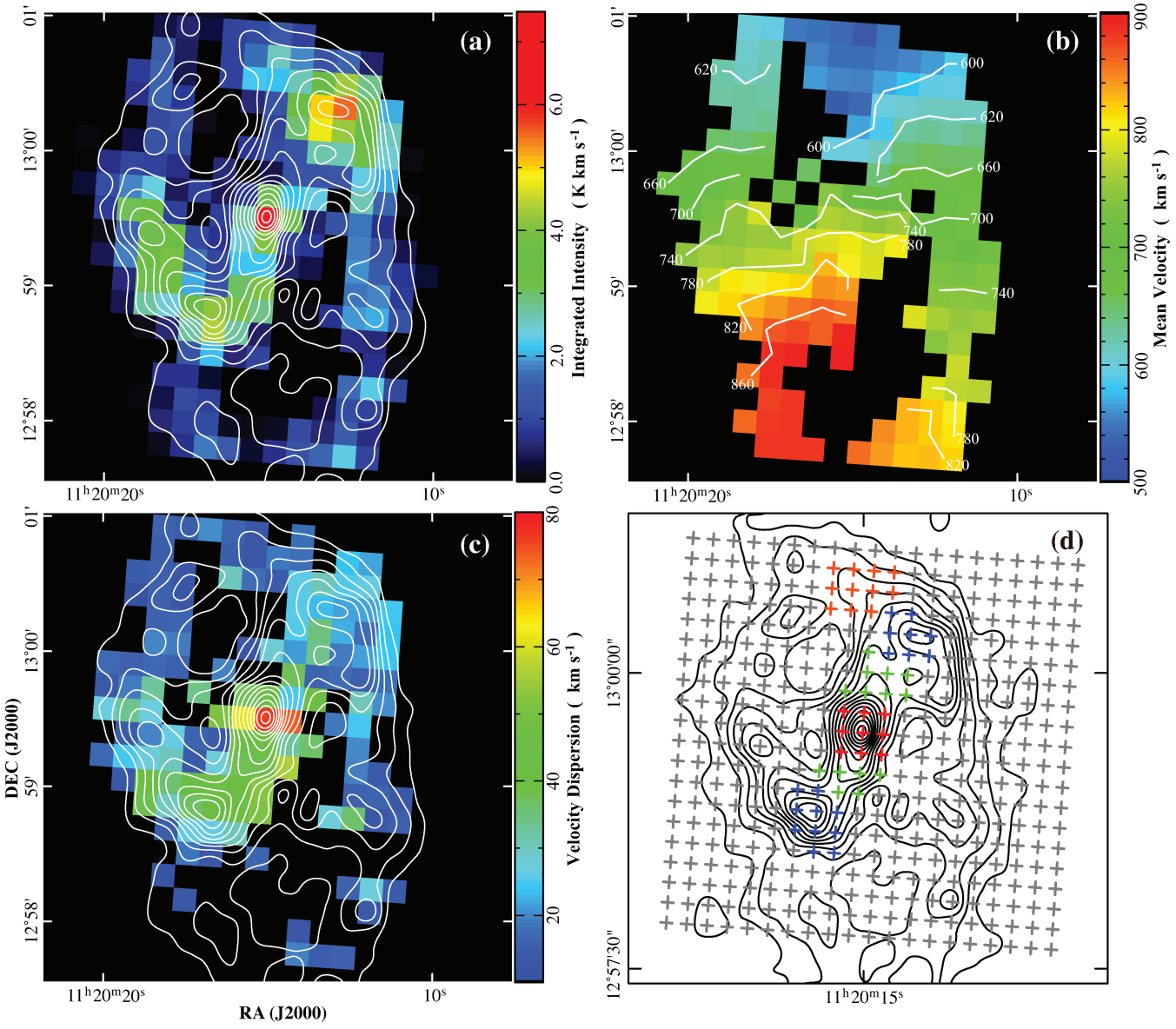

Figure 1. Colour map of (a) integrated intensity (zeroth moment), (b) velocity field (first moment) and (c) velocity dispersion (second moment) in NGC 3627 and observed positions. Contours of integrated intensity of ^{12}CO ($J = 1$–0) taken by Kuno et al. (2007) are overlaid on (a), (c) and (d). The contour levels are 5, 12, . . . , 110 K km s^{-1} with a step of 7 K km s^{-1}. In (d), the characteristic galactic structures are represented as different shades, in colour in the online journal: the central region (red), bar (green), bar ends (blue), offset streams (orange) and other regions, which mostly consist of the spiral arms.

molecular clouds spatially. Indeed, $R_{12/13}$ is found to be large in the Galactic molecular cloud, if $R_{12/13}$ is calculated from an averaged value of ^{12}CO and ^{13}CO integrated intensity over the entire region of the molecular cloud that is detected in ^{12}CO (Polk et al. 1988; Lee, Snell & Dickman 1990; Carpenter, Snell & Schloerb 1995).

Fig. 3 shows a map of $R_{12/13}$. The $R_{12/13}$ values were obtained only for positions where the intensity I_{13} is higher than three times ΔI_{13}, and only ΔI_{12} and ΔI_{13} are taken into account to derive the uncertainty $\Delta R_{12/13}$. As we expected, $R_{12/13}$ tends to be higher in central positions and in the bar than in other regions. The frequency distribution chart of $R_{12/13}$ for representative galactic locations (Fig. 4) and the averaged $R_{12/13}$ (Table 2) also clearly show these trends.

Previous work has indicated that $R_{12/13} = 11.2 \pm 1.2 \pm 5.7$ (the first uncertainty is based on rms noise and the second is based on the systematic uncertainty) in the central 45 arcsec of NGC 3627 (Paglione et al. 2001) and 15 ± 1 in the central 57 arcsec of the galaxy (Sage & Isbell 1991). Our $R_{12/13}$ is 15.6 ± 1.6 at the central pixel which agrees well with the values of previous works within the uncertainty.

4.2 Radial gradient of $R_{12/13}$

We find that $R_{12/13}$ decreases with distance from the galactic centre (Fig. 5). The overlaid solid straight line is obtained through the least-squares fit for the whole data set excluding positions in the centre and the bar. The slope of the line is -1.4 ± 0.4 kpc^{-1} and the intercept of the vertical axis is 14.1 ± 1.4. We excluded the positions of the central region and the bar when fitting the linear line in Fig. 5, since $R_{12/13}$ seems to be enhanced in these regions in comparison with the other regions. This would be caused by physical environment, such as nuclear activity. Moreover, the physical

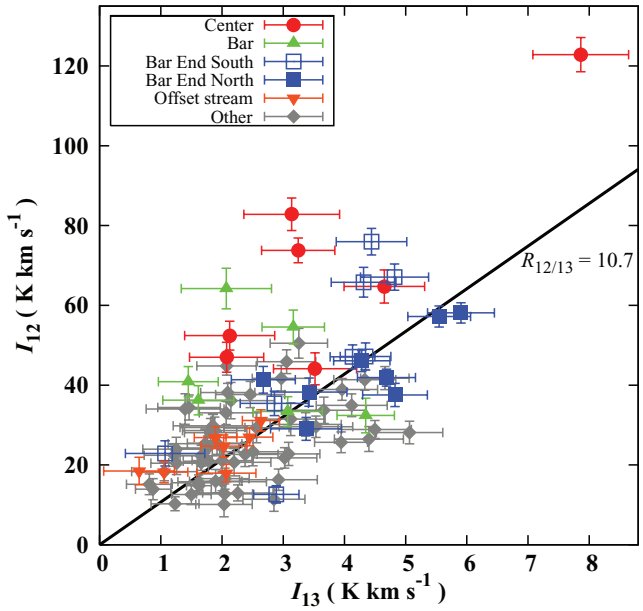

Figure 2. Plot of I_{12} versus I_{13} . I_{12} is shown in the central region (filled circle), bar (filled triangle), southern bar end (open square), northern bar end (filled square), offset stream (filled inverted triangle) and other regions (filled diamond) where most of the detected positions belong to the spiral arms. The least-squares fitting straight line for all data is shown by a solid line with a slope of 10.7 ± 0.4.

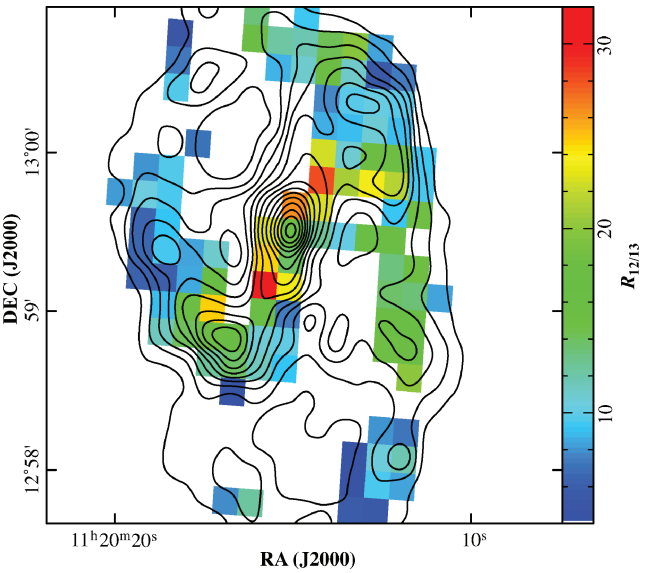

Figure 3. $R_{12/13}$ colour map of NGC 3627. Contours are the integrated intensity of ^{12}CO.

condition of the molecular gas in the bar is possibly different from that in the spiral arms, as we discuss later.

This result contradicts Paglione et al. (2001), since they have reported a negative gradient of $R_{12/13}$. The discrepancy may come from a beam-dilution effect and/or a smaller number of sample positions. Paglione et al. (2001) only observed along the major axis with a large spatial resolution of ∼45 arcsec. On the other hand, the spatial resolution of our observations is enough small to resolve individual structures, such as the bar ends, and our data consist of a sample number that is greater by an order of magnitude.

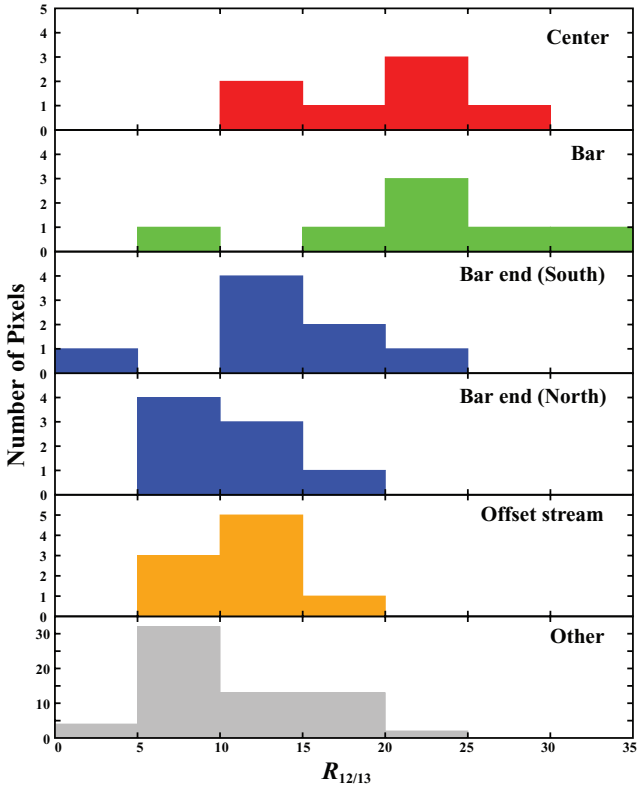

Figure 4. Frequency distribution of $R_{12/13}$ as a function of the specific location in the galaxy. The horizontal axis is $R_{12/13}$ and the vertical axis is the number of pixels.

The gradient of $R_{12/13}$ has been observed in some galaxies (Rickard & Blitz 1985; Young & Sanders 1986; Paglione et al. 2001). Paglione et al. (2001) have found the radial gradient of $R_{12/13}$ and discussed the variations in the relative ^{12}CO ($J = 1$–0) and ^{13}CO ($J = 1$–0) abundances and molecular gas properties, such as temperature, column density and velocity dispersion, as the possible causes of variation in $R_{12/13}$. They have concluded that a modest rise in kinetic temperature toward the nucleus from 2 kpc outside can account for the observed gradient using the non-local thermal equilibrium calculation with a single-component model. If our observed $R_{12/13}$ gradient is caused by the rise of the molecular gas kinetic temperature as Paglione et al. (2001) suggested, the interstellar radiation of field stars or star formations induced by spiral shocks are possible origins for the gas heating.

4.3 ^{13}CO($J = 1$–0) depletion in the bar

In the bar, we found that $R_{12/13}$ is twice as high as the average value of ∼10. As discussed in Paglione et al. (2001), due to the higher optical depth of ^{12}CO ($J = 1$–0),$R_{12/13}$ is sensitive to the optical depth of ^{13}CO ($J = 1$–0). In the local thermodynamic equilibrium (LTE) approximation, the optical depth of ^{13}CO ($J = 1$–0) is proportional to $N_{^{13}\mathrm{CO}}/\Delta V\ T_{\mathrm{k}}^2$, where $N_{^{13}\mathrm{CO}}$ is the column density of ^{13}CO, ΔV is the velocity dispersion and T_{k} is the kinetic temperature. Therefore there are at least three possible reasons for this high value: (1) higher kinematic temperature T_{k}, (2) smaller ^{13}CO column density and (3) larger velocity dispersion ΔV.

It is unlikely that the higher $R_{12/13}$ in the bar is due to higher temperature of molecular gas than the other regions. As we will show in the next section, there is no strong star-formation

Table 2. Averaged $R_{12/13}$, SFR and SFE.

Positions	$R_{12/13}$	Σ_{SFR} [$M_\odot$ kpc^{-2} yr^{-1}]	SFE [10^{-9} yr^{-1}]
Centre	17.3 ± 2.0	0.072 ± 0.005	1.23 ± 0.13
Bar	18.0 ± 2.3	0.028 ± 0.002	0.77 ± 0.11
Southern bar end	12.2 ± 1.0	0.149 ± 0.012	2.59 ± 0.27
Northern bar end	9.2 ± 0.6	0.100 ± 0.007	1.65 ± 0.16
Offset stream	10.4 ± 1.1	0.057 ± 0.004	1.80 ± 0.27
Other (mainly arms)	10.7 ± 0.4	0.027 ± 0.001	0.78 ± 0.05

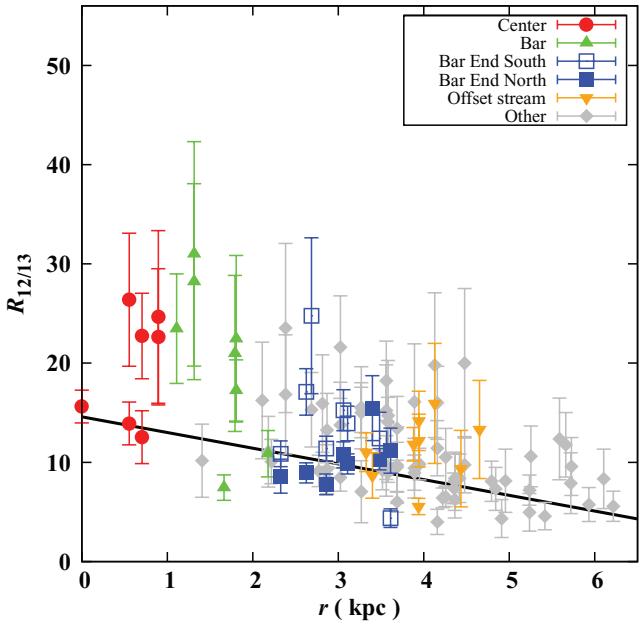

Figure 5. $R_{12/13}$ versus galactocentric distance (r). Symbols and shades are same as in Fig. 2.

activity, which is a possible heating source of molecular clouds in the bar, while in the bar ends, where strong star-formation activity can be seen, $R_{12/13}$ is lower than in the bar. This result suggests that star-formation feedback seems to have only a little effect on the temperature of the molecular cloud. Strong shock waves are expected in the bar but the shock wave cannot account for the rise of the molecular cloud temperature either, since the temperature rapidly decreases with a time-scale of $\sim 10^{2-3}$yr through radiative cooling, even if molecular clouds are temporarily heated by the shock. A continuous heating mechanism is needed to maintain the high temperature of the molecular cloud. Therefore it is possible to dismiss temperature variation as the origin of the higher $R_{12/13}$ in the bar.

Fig. 1(c) clearly shows higher velocity dispersion in the bar than in the other regions. Although the velocity dispersion mainly originates from the relative motion between the molecular clouds, a ^{12}CO photon can escape through molecular clouds which move with different velocity on the line of sight. Therefore the large velocity dispersion may explain a rise in $R_{12/13}$ in the bar.

The third reason, lower N_{13CO}, is also possible in the bar. Hüttemeister et al. (2000) suggested that the high $R_{12/13}$ is possibly caused by the contribution of a diffuse molecular component that is gravitationally unbound and has a moderate optical depth in ^{12}CO ($J = 1$–0). It is likely that the fraction of diffuse molecular gas that is too diffuse to emit in ^{13}CO ($J = 1$–0) but weakly emits in ^{12}CO ($J = 1$–0) is larger in the bar than in the other regions. A strong shear motion or shock wave breaks the molecular clouds into smaller and more diffuse ones in the bar, although some portion of the molecular gas may be compressed to be dense. The dispersed molecular gas, which has too inadequate a column density to be detected in ^{13}CO ($J = 1$–0) and is possibly gravitationally unbound, is spread in the bar. As a result, the beam-filling factor of ^{12}CO ($J = 1$–0) is much larger than that of ^{13}CO ($J = 1$–0) within the observed beam; also the column density of ^{13}CO is decreased. Moreover, in the case of ^{12}CO ($J = 1$–0), the intensity would be enhanced by a large velocity gradient, since the gradient increases the photon-escap probability of ^{12}CO ($J = 1$–0). The larger velocity gradient, as shown in Fig. 1(c), causes the emergence of ^{12}CO ($J = 1$–0) from deeper inside the molecular cloud, whilst in a cloud with smaller velocity gradient these photons are captured by other ^{12}CO before reaching the surface of the molecular cloud. Hence the higher $R_{12/13}$ indicates that we may overestimate the molecular gas mass calculated from ^{12}CO ($J = 1$–0) with the assumption of a standard CO-to-H_2 conversion factor. The contribution of this diffuse molecular gas to the total molecular gas mass is possibly small.

5 MOLECULAR GAS AND STAR-FORMATION ACTIVITY

5.1 Star-formation rate and molecular gas mass

As discussed in many previous studies, the molecular gas content plays an important role in star formation. In order to examine the relationship between molecular gas and star-formation activity in NGC 3627, we derived the density of the star-formation rate (Σ_{SFR}) from Hα and 24-μm data and compared it with the surface density of the molecular gas mass. We applied the calibration of the star-formation rate given by Calzetti et al. (2007) as follows:

$$SFR = 3.5 \times 10^{-42} \times [L(\mathrm{H}\alpha)_{\mathrm{obs}} + (0.031 \pm 0.006) \times L(24\,\mu\mathrm{m})]\,\mathrm{M}_\odot\,\mathrm{yr}^{-1}, \quad (1)$$

where $L(\mathrm{H}\alpha)_{\mathrm{obs}}$ is the luminosity of Hα in erg s^{-1} without the dust-extinction correction and $L(24\,\mu\mathrm{m})$ is the luminosity at 24 μm in erg s^{-1}. We utilized archival Hα and 24-μm data which are provided by the *Spitzer* Nearby Galaxies Survey (SINGS; Kennicutt et al. 2003).

The surface density of the molecular gas mass is calculated using the LTE approximation. We obtained the column density of $N_{^{13}CO}$ by

$$N_{^{13}CO} = \frac{3k_B}{4\pi^3 \nu_0 \mu^2} \frac{\int T_{\mathrm{MB}}(^{13}\mathrm{CO})\mathrm{d}v}{1 - \exp[-(h\nu_0)/(k_B T_k)]}\,\mathrm{cm}^{-2}, \quad (2)$$

where k_B is the Boltzmann constant, ν_0 is the rest frequency of ^{13}CO ($J = 1$–0), μ is the permanent dipole moment of ^{13}CO ($\mu = 0.11$ debye), h is Planck's constant and T_k is the kinetic temperature of the molecular gas. The surface density of the molecular gas mass

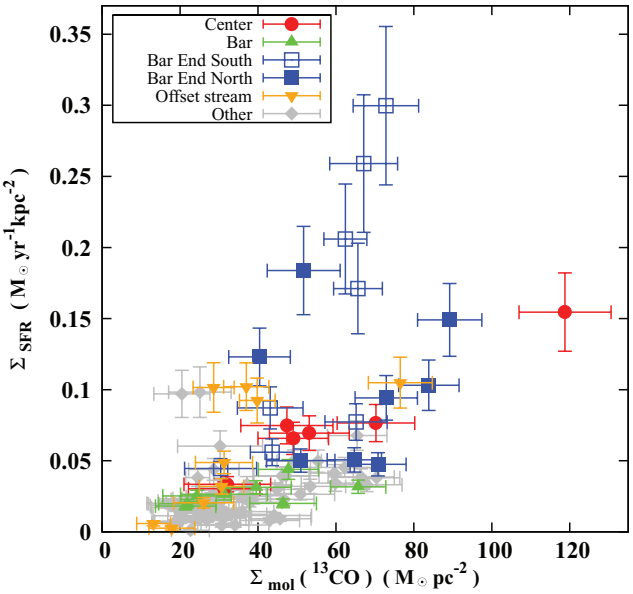

Figure 6. Correlation plot of the surface density of molecular gas derived from I_{13} ($\Sigma_{\rm mol}$) and the surface density of SFR ($\Sigma_{\rm SFR}$). The figure symbols and shades are same as in Fig. 2.

is given by

$$\Sigma_{\rm mol} = 15.1 \times \int T_{\rm MB}(^{13}{\rm CO}){\rm d}v \quad {\rm M}_\odot\,{\rm pc}^{-2}. \tag{3}$$

Here we adopted the ratio $N_{\rm H_2}/N_{^{13}{\rm CO}}$ of 7.5×10^5 (Frerking, Langer & Wilson 1982) and assumed that the kinetic temperature of the molecular gas is constant at $T_{\rm k} = 20$ K over the galaxy. We multiplied by a factor of 1.36 to account for the contribution of He by mass. The averaged SFR and SFE, which is the ratio $\Sigma_{\rm SFR}/\Sigma_{\rm mol}$ and indicates the time-scale of molecular gas consumption by star formation, in each galactic structure are summarized in Table 2.

As shown in Fig. 6, two series of positive correlation are seen between the surface density of the molecular gas mass derived from I_{13} and the surface density of the star-formation rate $\Sigma_{\rm SFR}$. The slope in Fig. 6 corresponds to the SFE: a steeper slope suggests higher SFE. The steeper slope is constituted mainly by the bar ends and the offset streams while other positions constitute the moderate slope.

Fig. 7 shows the radial distribution of SFE. As we indicated, the SFE appears to be a few times higher in the two bar ends and the offset stream than at other positions. As a whole, the SFE seems to decrease gradually with radius, excepting positions in the bar ends and the offset stream.

Fig. 8 shows that $R_{12/13}$ moderately increases with SFE in the two bar ends. It is possible that stellar feedback from OB stars causes a rise in the kinetic temperature of the molecular gas and makes the $R_{12/13}$ ratio higher. On the other hand, SFE is lower in the bar than that in the bar ends, although $R_{12/13}$ is much higher in the bar than both of the averaged $R_{12/13}$ over the whole galaxy and that in the bar ends. This result suggests, as already mentioned, that a rise in the kinetic temperature cannot be caused by star-formation activity in the bar and cannot account for the observed high $R_{12/13}$.

Some barred galaxies have low star-formation activity in their bars, although a large amount of molecular gas was observed in the ^{12}CO ($J = 1$–0) emission line. In NGC 3627, the SFE derived from ^{12}CO ($J = 1$–0) is also 1.6 times lower than in the spiral arms. However, we found that the SFE derived from ^{13}CO ($J = 1$–0) is comparable to that derived from ^{12}CO ($J = 1$–0) in these two

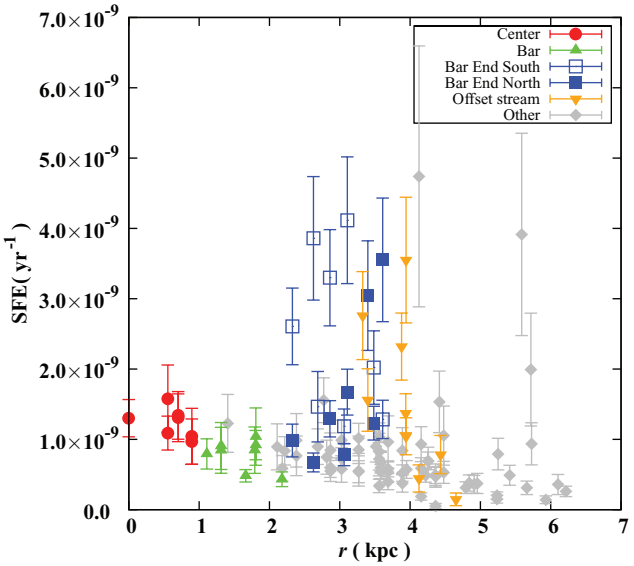

Figure 7. Radial distribution of SFE derived from ^{13}CO ($J = 1$–0). Symbols and colour are the same as in Fig. 2.

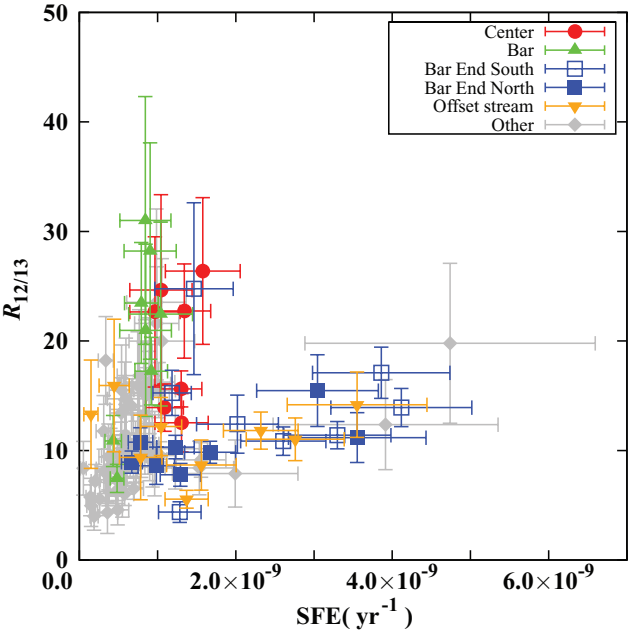

Figure 8. $R_{12/13}$ as a function of SFE. The representations of figure symbols and shades are the same as in Fig. 2.

regions. This discrepancy comes from differences of $R_{12/13}$ between the bar and the spiral arms. Since ^{13}CO ($J = 1$–0) is a better tracer of molecular gas mass than ^{12}CO ($J = 1$–0), SFE derived from ^{13}CO ($J = 1$–0) is more reliable. Our result might imply that dynamical phenomena expected in the bar, such as shock waves and string shear motion, have little impact on star formation in individual molecular clouds in the bar.

5.2 Star-formation efficiency in the bar ends

It is clear that SFE is enhanced in the two bar ends and the offset stream compared with the other positions, as mentioned above, even

if $R_{12/13}$ is taken into account. There are at least two possible reasons why SFE might be boosted in these regions.

(i) $\Sigma_{\rm mol}$ is underestimated. If the kinetic temperature increases, the conversion factor calculated in equation (2) also increases.
(ii) Stars are actually formed efficiently.

In the following sections, we will provide some discussions of the above possibilities.

5.2.1 *Conversion factor of* ^{13}CO ($J = 1$–0)

In this subsection we examine possibility (i) in more detail. In Fig. 8, we found that $R_{12/13}$ slightly increases with an increase of SFE in the bar ends. The correlation could be explained by a rise in the kinetic temperature caused by feedback from OB stars. We assumed a constant kinetic temperature $T_{\rm k} = 20$ K over the galaxy and calculated the conversion factor of ^{13}CO ($J = 1$–0) in equation (2). Let us assume $T_{\rm k} = 40$ K; the conversion factor of ^{13}CO ($J = 1$–0) is then increased by a factor of 1.9. If this conversion factor is adopted, the molecular gas mass surface density is increased and the averaged SFE is decreased to $\sim(1.36 \pm 0.14) \times 10^{-9}$ yr^{-1} in the southern bar end and $\sim(0.8 \pm 0.08) \times 10^{-9}$ yr^{-1} in the northern bar end. The derived SFE is comparable to the averaged values in the other regions (mainly arms) and if this is the case then galactic-scale stellar bar structure has no impact on the local star-formation process, but only assembles molecular clouds in the bar ends. However, observations of higher rotational CO transitions are necessary to conclude that the kinetic temperature is higher and SFE is, thus, comparable in the bar ends and the arms.

5.2.2 *Gravitational instability*

We found that the bar ends are the positions where a greater molecular gas mass is assembled than in the spiral arms and the bar. Gravitational instability of the molecular gas or an increase in the cloud–cloud collision rate is expected under the gas-rich environment of the bar ends, because these two are possible mechanisms of star-formation enhancement. In this section, we compare the Toomre Q-parameter with the star-formation efficiency and examine possibility (ii).

The Toomre Q-parameter (Toomre 1964; Goldreich & Lynden-Bell 1965) gives the ring-mode gravitational stability of a self-gravitating disc, where a smaller Q-parameter than unity indicates an unstable disc. The Toomre Q-parameter is defined such that

$$Q = \frac{\kappa\sigma}{\pi G \Sigma_{\rm gas}}, \tag{4}$$

where σ is the gas velocity dispersion, G is the gravitational constant, $\Sigma_{\rm gas}$ the surface density of gas and κ is the epicycle frequency:

$$\kappa(r) = \left[2\frac{V_{\rm rot}(r)}{r}\left(\frac{V_{\rm rot}(r)}{r} + \frac{{\rm d}V_{\rm rot}}{{\rm d}r}\right)\right]^{\frac{1}{2}}, \tag{5}$$

where $V_{\rm rot}(r)$ is the rotation velocity.

In order to calculate κ in equation (4), we obtained a rotation curve from ^{12}CO ($J = 1$–0) data following the method given in Sofue (1996). Terminal velocities were obtained along the major axis and averaged at the same radius. We adopted a system velocity ($V_{\rm sys}$) of 715 km s^{-1}, position angle (PA) of 176° and inclination angle (IA) of 52° (Kuno et al. 2007). The upper panel in Fig. 9 shows the terminal velocities and rotation curve obtained. Slight asymmetries are recognizable in the terminal velocities inside the bar between radii of 1.6 kpc and 3.3 kpc, possibly due to non-circular gas motion induced by the bar potential (Chemin et al. 2003).

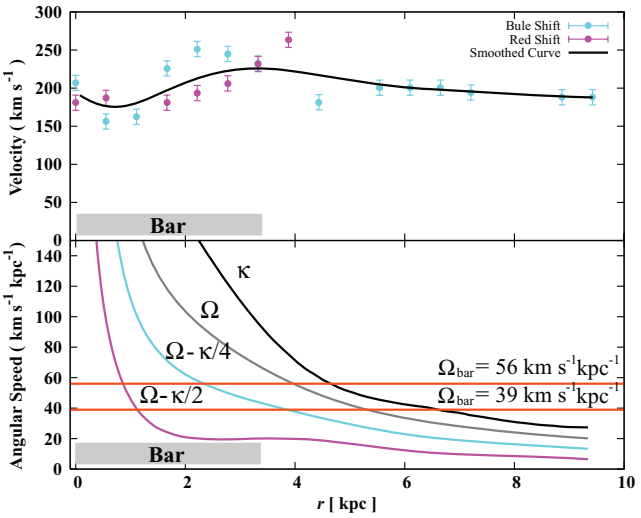

Figure 9. Upper panel: The black curve is the obtained rotation curve. The shaded plots (colour in the online journal) are the terminal velocity in the northern and southern disc. Lower panel: Angular velocity Ω and epicyclic frequency κ as a function of galactocentric distance. $\Omega - \kappa/2$ and $\Omega - \kappa/4$ are also shown in the panel. The grey thick underline shows the bar radius (3.4 kpc) obtained by fitting an ellipse to the 2MASS *Ks*-band image. The horizontal lines (orange in the online journal) indicate the pattern speed of the bar in our study (56 km s^{-1} kpc^{-1}) and that of Hirota et al. 2009 (39 km s^{-1} kpc^{-1}).

The lower panel of Fig. 9 shows the angular velocity ($\Omega(r) = V_{\rm rot}(r)/r$) and the epicyclic frequency κ as a function of radius. The typical uncertainty in the angular velocity is about 10 km s^{-1} kpc^{-1}, which is given by d$V_{\rm rot}$ and dr. The radius of the bar shown in Fig. 9 was obtained using a 2MASS $K_{\rm s}$-band image (Jarrett et al. 2003) and fitting the isophotes with ellipses using IRAF STSDAS task ELLIPS. We defined the radius of the bar as the location of maximum ellipticity ($\epsilon = 1 - b/a$, where a is the major axis of the ellipse and b is the minor axis of the ellipse). The measured bar radius is 60 arcsec and the length of the deprojected bar is ∼3.4 kpc at a distance of 11.1 Mpc.

Fig. 10 shows a correlation plot between the calculated Q-parameter and SFE. We consider only the surface density of molecular gas, $\Sigma_{\rm gas} = \Sigma_{\rm mol}(^{13}{\rm CO})$, and we adopt a typical value of ∼10 km s^{-1} (Sakamoto et al. 1999) for the velocity dispersion σ. We found that most positions that show SFE enhancement have $Q \sim 1$, while Q varies from ∼1 to ∼6.5 at the positions where SFE is smaller than $\sim 1.5 \times 10^{-9}$ yr^{-1}. This result may imply that gravitational instability promotes star formation in the bar ends.

However, there are some positions where the Q-parameter is unity with no star-formation enhancement. Koda et al. (2005) have suggested that the Q-parameter from CO observation indicates neither star formation nor molecular cloud formation, from their CO observation of early-type spiral galaxies and the suggestion that cloud–cloud collisions might account for star-formation activities. It is also unknown whether the Q-parameter is applicable to barred galaxies as a gravitational stability criterion, since the Q-parameter gives the stability of a disc with constant surface density while discs of barred galaxies contain asymmetric structures such as a bar and spiral arms. Thus a Q-parameter of unity possibly reflects an increased surface density of molecular gas due to other reasons, e.g. orbital resonance or orbit crowding.

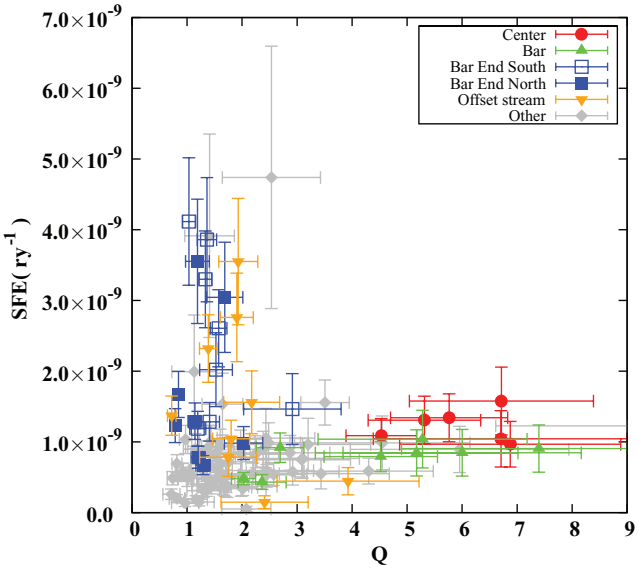

Figure 10. Correlation plot of the Toomre Q-parameter and SFE. Symbols and shades are the same as in Fig. 2.

In order to examine orbital resonances, we estimated the pattern speed of the bar, $\Omega_{\rm bar} = 53 \pm 12\,{\rm km\,s^{-1}\,kpc^{-1}}$, assuming that a corotation radius resides in the radius of 1.2 times the length of the bar major axis (∼4.1 kpc), which is the mean value of the corotation radii measured in other galaxies (Michel-Dansac & Wozniak 2006). The pattern speed of the bar in NGC 3627 has also been estimated by several studies: 56 km s^{-1} kpc^{-1} (Chemin et al. 2003), 55 km s^{-1} kpc^{-1} (Sheth et al. 2002), 50^{+3}_{-8} km s^{-1} kpc^{-1} (Helfer et al. 2003) and 39 km s^{-1} kpc^{-1} (Hirota et al. 2009). These pattern speeds are comparable to our pattern speed, excepting the case of Hirota et al. (2009). In this estimation we assumed only circular motion, however radial inflow motion is expected in the bar. If radial inflow motion exists, we find by considering the inclination angle that the line-of-sight velocity is more redshifted in the southern half of the bar and more blueshifted in the northern bar. Therefore the pattern speed of the bar is estimated to be slower if radial inflow is taken into account. Hirota et al. (2009) have measured the pattern speed by utilizing a method that take advantage of the nature of the streaming motion caused by the bar potential, proposed by Kuno et al. (2000). Therefore the pattern speed of the bar, $\Omega_{\rm bar}$, exists between 39 km s^{-1} kpc^{-1} and 56 km s^{-1} kpc^{-1}. Fig. 9 shows that an ultraharmonic resonance (UHR), which forms an inner ring, may be located between 2.4 kpc and 3.9 kpc in the vicinity of the bar ends, since the bar pattern speed ($\Omega_{\rm bar}$) meets the curve of $\Omega - \kappa/4$. The UHR is one potential mechanism to populate the molecular gas and to increase the surface density of the bar ends. Populated gas related to UHR has been found in NGC 4579 (García-Burillo et al. 2009).

Orbit-crowding, however, is also another potential mechanism to populate the molecular gas in the bar ends. The results of Regan et al. (1999) indicate streaming gas motion along the bar from the bar ends to the bar in NGC 3627. Orbit crowding implies streaming motion (Kenney & Lord 1991) and also increases the surface density of the molecular gas in the bar.

If the Q-parameter indicates gravitational instability and this instability influences star formation, we might expect the following scenario. Our observation beam size of ∼900 pc contains many giant molecular clouds (GMCs) with sizes ∼10 pc and $\Sigma_{\rm mol}(^{13}{\rm CO})$ is proportional to the number density of GMCs. We can consider the observed CO emission as not molecular gas fluid but an ensemble of GMCs or a fluid of GMCs. The Q-parameter we derived gives the gravitational stability of the assembly of GMCs, since the Toomre stability criterion is almost the same form of equation (4) as for stars, the difference being the constant, π and 3.36, in the denominator of equation (4).

Thus gravitational instability of an assembly of molecular clouds occurs after the molecular clouds are gathered at the bar ends through resonance and/or orbit crowding. The gravitational instability compresses the assembly of GMCs and confines them within a smaller area. As a result, the probability of cloud–cloud collision is increased and the star-formation activity is enhanced in the bar ends. The critical surface density ($\Sigma_{\rm crit} = \kappa\sigma/\pi G$) decreases with radius, since the epicyclic frequency κ decreases with radius. Thus, at the outer regions, the surface density of molecular clouds is lower, even if Q is nearly unity. The low surface density increases on the timescale of cloud–cloud collisions, which is proportional to the inverse of the number density of molecular clouds. This may be the reason for the lower Q-parameter with no star-formation enhancement in this scenario.

6 CONCLUSIONS

We present mapping observations of the ^{13}CO (J = 1–0) emission line from the barred spiral galaxy NGC 3627 with the Nobayama 45-m telescope. The main results are as follows.

(i) $R_{12/13}$ is as high as about 20 in the bar compared with the averaged value of ∼10. This result implies that the contribution of gravitationally unbound diffuse gas is large and the molecular gas mass obtained from ^{12}CO (J = 1–0) with the standard conversion factor is overestimated in the bar.

(ii) Since $R_{12/13}$ is high in the bar, the SFE calculated from ^{13}CO (J = 1–0) is larger than that calculated from ^{12}CO (J = 1–0) in the bar. Moreover, the SFE calculated from ^{13}CO (J = 1–0) in the bar is similar to that in the disc, although SFE have been suggested to be low in the bar. This discrepancy is caused by the overestimation of molecular gas mass calculated from ^{12}CO (J = 1–0). Because of the fact that ^{13}CO (J = 1–0) traces the column density of molecular gas more precisely than ^{12}CO (J = 1–0), it is now established that there is no difference in SFE between the bar and the disc.

(iii) We found that $R_{12/13}$ decreases with galactocentric distance at a rate of $-1.4 \pm 0.4\,{\rm kpc^{-1}}$. This gradient is recognizable even if the nuclear region and the bar are excepted.

(iv) SFE calculated from ^{13}CO (J = 1–0) in the bar ends tends to be larger than in other regions. In these regions, the Toomre Q-parameter is about unity and one possible reason for this SFE enhancement is that the gravitational instability of an assembly of molecular clouds enhances cloud–cloud collisions and the formation of dense molecular gas.

ACKNOWLEDGMENTS

This publication makes use of data products from the Two Micron All Sky Survey, which is a joint project of the University of Massachusetts and the Infrared Processing and Analysis Center/California Institute of Technology, funded by the National Aeronautics and Space Administration and the National Science Foundation. This investigation is financially supported in part by the National Astronomical Observatory of Japan.

Nobeyama Radio Observatory is a branch of the National Astronomical Observatory of Japan, National Institutes of Natural Sciences.

REFERENCES

Athanassoula E., 1992, MNRAS, 259, 345
Calzetti D. et al., 2007, ApJ, 666, 870
Carpenter J. M., Snell R. L., Schloerb F. P., 1995, ApJ, 445, 246
Chemin L., Cayatte V., Balkowski C., Marcelin M., Amram P., van Driel W., Flores H., 2003, A&A, 405, 89
de Vaucouleurs G., de Vaucouleurs A., Corwin H. G., Jr, Buta R. J., Paturel G., Fouque P., 1991, Third Reference Catalogue of Bright Galaxies. Springer-Verlag, Berlin
Frerking M. A., Langer W. D., Wilson R. W., 1982, ApJ, 262, 590
García-Burillo S. et al., 2009, A&A, 496, 85
Goldreich P., Lynden-Bell D., 1965, MNRAS, 130, 125
Haynes M. P., Giovanelli R., Roberts M. S., 1979, AJ, 229, 83
Helfer T. T., Thornley M. D., Regan M. W., Wong T., Sheth K., Vogel S. N., Blitz L., Bock D. C.-J., 2003, ApJS, 145, 259
Hirota A., Kuno N., Sato N., Nakanishi H., Tosaki T., Matsui H., Habe A., Sorai K., 2009, PASJ, 61, 441
Ho L. C., Filippenko A. V., Sargent W. L. W., 1997, ApJS, 112, 315
Hüttemeister S., Aalto S., Das M., Wall W. F., 2000, A&A, 363, 93
Jarrett T. H., Chester T., Cutri R., Schneider S. F., Huchra J. P., 2003, AJ, 125, 525.
Kenney J. D. P., Lord D. S., 1991, ApJ, 381, 118
Kennicutt R. C. et al., 2003, PASP, 115, 928
Koda J., Okuda T., Nakanishi K., Kohno K., Ishizuki S., Kuno N., Okumura S. K., 2005, A&A, 431, 887
Kuno N., Nishiyama K., Nakai N., Sorai K., Vila-Vilaró B., Handa T., 2000, PASJ, 52, 775
Kuno N. et al., 2007, PASJ, 59, 117
Lee Y., Snell R. L., Dickman R. L., 1990, ApJ, 355, 536
Michel-Dansac L., Wozniak H., 2006, A&A, 452, 97
Paglione T. A. D. et al., 2001, ApJS, 135, 183
Polk K. S., Knapp G. R., Stark A. A., Wilson R. W., 1988, ApJ, 332, 432
Regan M. W., Sheth K., Vogel S. N., 1999, ApJ, 526, 97
Reuter H.-P., Sievers A. W., Pohl M., Lesch H., Wielebinski R., 1996, A&A, 306, 721
Reynaud T., Downes D., 1998, A&A, 331, 671
Rickard L. J., Blitz L., 1985, ApJ, 292, L57
Roberts W. W., Jr, Huntley J. M., van Albada G. D., 1979, ApJ, 233, 67
Sage L. J., Isbel D. W., 1991, A&A, 247, 320
Saha A., Sandage A., Tammann G. A., Labhardt L., Macchetto F. D., Panagia N., 1999, ApJ, 522, 802
Sakamoto K., Okumura S. K., Ishizuki S., Scoville N. Z., 1999, ApJ, 525, 691
Sheth K., Regan M. W., Vogel S. N., Teuben P. J., 2000, ApJ, 532, 221
Sheth K., Vogel S. N., Regan M. W., Teuben P. J., Harris A. I., Thornley M. D., 2002, AJ, 124, 2581
Sofue Y., 1996, ApJ, 458, 131
Sorai K., Sunada K., Okumura S. K., Iwasa T., Tanaka A., Natori K., Onuki H., 2000, SPIE, 4015, 86
Toomre A., 1964, ApJ, 139, 1217
Young J. S., Sanders D. B., 1986, ApJ, 302, 680

This paper has been typeset from a TEX/LATEX file prepared by the author.